Journal of Building Engineering 118 (2026) 114893

Contents lists available at ScienceDirect

Journal of Building Engineering

journal homepage: www.elsevier.com/locate/jobe

Full Length Article

Anomaly identification in historical modular structures using satellite data: Methodology and application to Portico di San Luca, Bologna

Wael Alahmad [a], Said Quqa [b,*], Francesco Ubertini [b], Cristina Gentilini [a]

[a] Department of Architecture, University of Bologna, Viale del Risorgimento 2, Bologna, 40136, Italy
[b] Department of Civil, Chemical, Environmental, and Materials Engineering, University of Bologna, Viale del Risorgimento 2, Bologna, 40136, Italy

ARTICLE INFO

Keywords:
Simplified structural model
Damage identification
Population-based structural health monitoring
Masonry arch

ABSTRACT

This paper presents a novel methodology for detecting and characterizing structural anomalies in historical modular structures using satellite-derived displacement data. The proposed framework monitors short-term correlations among statistical features of different structural segments and identifies anomalies as individual deviations from the collective behavior. Segments exhibiting such deviations are classified as anomalous and further characterized with the aid of a simplified parametric model that requires only basic geometric information. This strategy enables the transfer of knowledge from simulated damage scenarios to real-world cases without the need for detailed mechanical modeling. The methodology is applied to the Portico di San Luca in Bologna, Italy, a historic arcade recently designated as a UNESCO World Heritage Site. Detected anomalies are validated against average velocity maps, a conventional product in satellite-based structural health monitoring. Whereas velocity maps require multi-year datasets to estimate long-term trends, the proposed method computes an anomaly index at each acquisition, enabling near-real-time detection while explicitly filtering out environmental effects acting uniformly across the structure. The results demonstrate the potential of satellite-informed structural health monitoring at the regional scale, offering a scalable, non-invasive, and cost-effective tool for the preservation and preventive maintenance of cultural heritage assets.

1. Introduction

Historical structures stand as enduring symbols of human ingenuity and cultural heritage. From ancient stone bridges to iconic landmarks, they have withstood the test of time, shaping the identities of cities and nations. However, aging materials, increased usage, and environmental changes pose growing threats to their conservation. The protection of these irreplaceable assets requires innovative and cost-effective monitoring strategies.

Structural health monitoring (SHM) provides valuable information on the condition of civil structures and historical monuments through nondestructive methods [1–5]. However, traditional SHM techniques often involve high costs due to on-site sensor deployment and data management.

Interferometric Synthetic Aperture Radar (InSAR) offers a powerful alternative for detecting and quantifying ground and structural displacements with millimeter precision by analyzing phase differences in radar signals acquired over time [6–8]. Initially,

* Corresponding author.
E-mail address: said.quqa2@unibo.it (S. Quqa).

https://doi.org/10.1016/j.jobe.2025.114893
Received 13 May 2025; Received in revised form 3 November 2025; Accepted 5 December 2025
Available online 13 December 2025

InSAR was used primarily to monitor ground surface changes, such as subsidence and landslides [6,7], playing a crucial role in hazard assessment and mitigation. More recently, researchers have demonstrated its effectiveness in monitoring civil infrastructure and historical buildings.

In the context of heritage monitoring, Selvakumaran et al. [9] developed an approach to detect partial failures on the Tadcaster Bridge (England), identifying structural anomalies more than a month before collapse. Similarly, Gagliardi et al. [5] applied InSAR to monitor the Rochester Bridge (UK), successfully detecting areas prone to subsidence and downward displacement. Alani et al. [10] demonstrated the benefits of combining InSAR with ground penetration radar to assess the structural integrity of the 13th-century Aylesford masonry arch bridge (UK). Their study linked observed displacements with seasonal variations in water level, offering critical insight into the long-term stability of the bridge. Bonaldo et al. [11] applied InSAR to monitor Palazzo Primoli (Italy), a 16th-century structure, revealing long-term deformation trends by integrating satellite-based displacement analysis with on-site inspections.

Beyond SHM, recent studies have explored methodologies for predicting the remaining service life of structures experiencing slow deformation. Farneti et al. [12,13] introduced a multidisciplinary approach that combines InSAR displacement data with numerical collapse simulations using the applied element method. This methodology was applied to the Albiano-Magra bridge (Italy), which collapsed in April 2020. By integrating satellite-based monitoring with numerical modeling, the study analyzed the progressive failure mechanism of the bridge and provided an estimate of its residual service life. Although using numerical models has proved fundamental for interpreting structural anomalies, accurately modeling historical structures remains challenging due to uncertainties in their geometry and material properties.

Most studies employing satellite data for SHM have treated InSAR-derived displacements in a manner analogous to data from on-site sensors [9,10]. However, two key aspects differentiate satellite observations from traditional ground-based measurements. First, the location of persistent scatterers (PSs) (i.e., the points where displacement time histories are available) is affected by geolocation uncertainties and limited spatial resolution, especially compared to the typical size of civil structures and, more significantly, historical buildings [14]. These factors can complicate the direct association between measured points and specific structural components. Second, InSAR imagery offers global spatial coverage and extensive historical archives spanning several decades, allowing retrospective assessments of structures that have never been instrumented or monitored on site.

These distinctive characteristics make population-based SHM (PBSHM) particularly promising for InSAR applications [15,16]. PBSHM extends traditional SHM by exploiting statistical relationships across a population of structures, rather than relying solely on the historical data of a single asset. While structural differences often hinder direct comparison of their responses, PBSHM enables the transfer of knowledge between structures that share similar characteristics. In this framework, classifiers (such as those used for damage identification) can be trained using data from analogous structures, where larger and more diverse datasets, including damaged conditions, are typically available [17]. Building on this concept, Gardner et al. [18] introduced domain adaptation (DA) for vibration-based SHM, in which damage-sensitive features (e.g., natural frequencies) from different structures are projected into a common feature space, thereby allowing meaningful comparison and improved generalization across the structural population.

The first application of PBSHM with satellite data involved comparing multiple structures within the same geographic region (i.e., bridges along a river) that experience similar environmental conditions [15]. This approach enabled the detection of structure-specific anomalies while filtering out environmental influences that affect all structures collectively. Although PBSHM has shown strong potential for civil infrastructures, applying it to cultural heritage structures presents unique challenges due to their diverse designs and construction methods. Nevertheless, for structures with periodic repeating modules, such as bridges, walls, or arcades, PBSHM can be used effectively by treating individual modules or structural segments as "similar" units.

This paper presents a new methodology to:

- apply PBSHM to historical modular structures using satellite data, enabling the identification of structural anomalies in individual segments while accounting for environmental variations;
- develop simplified parametric models of the monitored structure to facilitate simulation-to-real knowledge transfer for anomaly characterization.

A key advantage of the proposed approach is that anomalies are identified through instantaneous comparisons among structural segments, eliminating the need for large historical datasets typically required by conventional InSAR-based SHM methods that rely on long-term velocity trend analyses. Additionally, the framework does not rely on the precise geolocation of the PSs, but instead derives global statistical features at the segment scale. Moreover, the simplified parametric model employed does not require detailed geometric or material information, which is often unavailable or highly uncertain for historical structures.

Building on these elements, DA techniques are used to align features between a synthetic source model and real structural segments, thereby reducing discrepancies between them. This alignment allows a classifier trained on simulated anomaly scenarios (where structural damages can be explicitly modeled) to infer potential anomalies in the real monitored structure.

After a description of an exemplary historical modular structure, the Portico di San Luca in Bologna, Italy (Section 2), and the satellite data used in this study (Section 3), this paper introduces a parametric model designed to capture structural displacements in response to environmental factors, specifically air temperature, humidity, and soil moisture (Section 4). This model is general and can simulate the response of various modular masonry structures, including arcades and masonry bridges. A novel procedure for InSAR-driven PBSHM is then presented, along with a strategy to use the proposed parametric model for anomaly characterization (Section 5). The proposed methodology is then applied to the selected case study (Section 6).

(a) (b) (c)

Fig. 1. Views of the Portico in April 2025: (a) Arco del Meloncello, (b) external view, (c) internal view.

2. Case study: the Portico di San Luca

The Portico di San Luca, located in Bologna, Italy, is a historical covered walkway that connects the city center (Porta Saragozza) to the Sanctuary of the Madonna di San Luca, atop Colle della Guardia. Constructed gradually over nearly a century, the structure was conceived in the mid-17th century to provide shelter for pilgrims during religious processions involving a revered icon of the Madonna [19–21].

Construction began in 1674, following architectural plans presented by Ercole Fichi and Camillo Saccenti and initially supervised by Giovanni Giacomo Monti. The initial flat portion, comprising 306 arches, was completed in 1701, stretching from the city center up to the foot of the hill at the Arco del Meloncello (Fig. 1(a)). Subsequently, architect Carlo Francesco Dotti designed the Arco del Meloncello, an iconic element marking the transition from the flat to the ascending hill section (Figs. 1(b,c)), completed in 1732. Additional segments of the uphill portion were built incrementally, finalizing the entire 3.8-kilometer structure, totaling 666 arches, by approximately 1739 [21]. Along the uphill portion, 15 chapels were also constructed, dedicated to the Mysteries of the Rosary (see circles I-XV in Fig. 2).

Over the following centuries, the Portico underwent multiple restorations and conservation efforts. Significant interventions occurred after structural damage, notably following the earthquake of 1768, for which the Portico required substantial repairs and structural consolidation throughout the late 18th century. Further restorations were carried out periodically, including major repairs in 1887–1888, addressing deterioration and renewing the structural integrity of walkway segments.

World War II and natural degradation led to additional restoration campaigns in the second half of the 20th century. In 1988, a dedicated Committee for the Restoration of the Portico di San Luca was established, aiming to organize preservation efforts. Significant restoration work took place in the year 2000 around the Arco del Meloncello, supported by community-driven fundraising associated with the Jubilee celebrations. In 2013, a crowdfunding campaign involving local citizens and international donors funded further comprehensive restoration. More recently, since 2014, additional preservation and restoration initiatives have continued to address structural and aesthetic concerns.

In 2021, recognizing its outstanding historical and cultural value, UNESCO officially designated the Portico di San Luca, along with other notable porticoes of Bologna, as a World Heritage site.

This study examines the hill portion as a representative example of a historical modular structure. Four structural segments with comparable geometries are defined. The first three segments encompass the arches within four consecutive Mysteries, while the fourth covers the uppermost portion of the Portico, located close to the Sanctuary. Fig. 2 provides an overview of the structure, the segmentation adopted in this study, and a schematic representation of a typical bay illustrating the approximate dimensions of its main elements.

3. Displacement and environmental data

The datasets used in this study include interferometric displacement measurements and environmental data, all retrieved via satellite observations.

Displacement data are sourced from the European Ground Motion Service [22], accessible through the Copernicus project, and derived from the Sentinel-1 satellite constellation. Sentinel-1 operates in the C-band at a central frequency of 5.405 GHz, corresponding to a wavelength of approximately 5.6 cm. In its interferometric wide swath (IW) mode, it achieves a ground resolution of 5 m in range (perpendicular to the travel direction) and 20 m in azimuth (parallel to the travel direction), with a swath width of 250 km. Specifically, this study uses the "calibrated product" (L2b) available on the EGMS portal. This product provides displacement time histories for stable, high-reflectivity ground points, known as persistent scatterers (PSs), identified using the PS-InSAR technique [7]. Displacements are measured along the line-of-sight (LOS) between the PS and the satellite, with the LOS inclination depending on the acquisition geometry. The L2b product is referenced to a GNSS-derived model, ensuring spatial

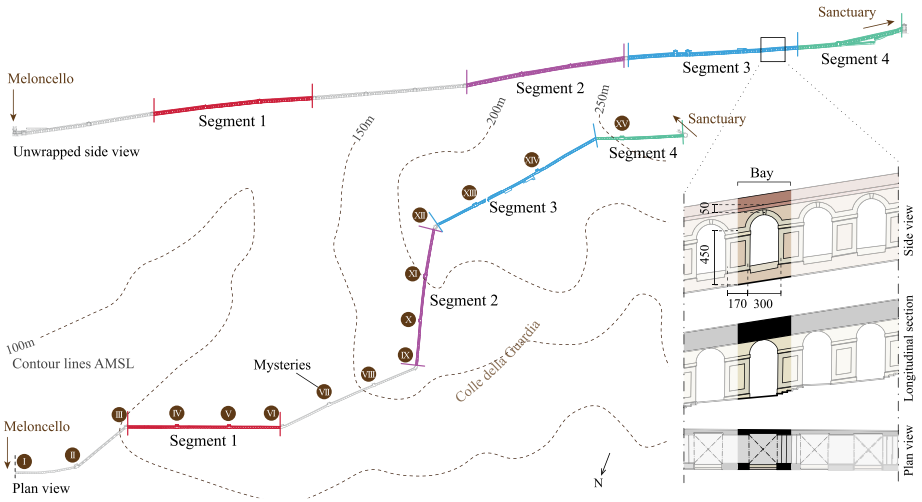

Fig. 2. Overall views of the portico structure and approximate size of a bay. Measures in cm.

consistency and absolute measurements across regions. It also incorporates preprocessing techniques such as atmospheric correction and phase unwrapping [14,23].

The principle of InSAR relies on comparing the phase of radar signals backscattered from the same ground target across repeated satellite acquisitions. The differences in phase represent changes in the travel path of the radar wave, which can be translated into relative displacements along the LOS. When long temporal series are analyzed, atmospheric disturbances and random noise are statistically filtered, enabling millimetric precision in ground-motion detection. According to the EGMS technical specifications, the standard deviation of individual LOS displacement measurements is approximately 8 mm, depending on coherence [14]. Although a single static GNSS station typically achieves higher absolute accuracy, InSAR provides vastly denser spatial coverage without the need for in-situ instrumentation. Its main limitation lies in the one-dimensional nature of LOS measurements, which require geometric decomposition to separate vertical and horizontal displacement components.

The displacement dataset analyzed in this study covers the period from April 15, 2018, to September 16, 2022. Temporal resolution within this interval varies: when both Sentinel-1 A and Sentinel-1B were operational, data were acquired every 6 days. After the in-flight anomaly of Sentinel-1B on December 23, 2021, the revisit cycle was extended to 12 days [24]. The data were acquired by the satellites during ascending orbits (south-to-north trajectory). Since Sentinel-1 captures images in bursts by cyclically switching the antenna beam across multiple adjacent "sub-swaths", variations in acquisition geometry (i.e., track and incidence angle) occur. In the region of the selected case study, the EGMS portal provides data for different satellite tracks and sub-swaths, namely track 117-IW1 and track 15-IW3, which are analyzed separately in this study.

Fig. 3 illustrates the spatial distribution of the PSs in the four analyzed segments for each satellite track. The structural portion between segment 1 and segment 2 was excluded from this analysis due to the limited number of PSs available. This limitation was likely due to the specific orientation of that segment, similar to segment 3, where a modest number of PSs are available. It is worth mentioning that the missing segment was classified as critical during previous evaluation campaigns. Therefore, future analyses will be conducted using high-resolution InSAR data obtained from other satellite constellations. The present work, however, focuses on validating the proposed methodology, which is designed to operate effectively using freely available datasets.

The environmental data considered in this study includes the temperature and relative humidity of the air measured at 2 m above the ground level and the moisture of the soil within the upper layer of 0–7 cm. These datasets are derived from satellite observations acquired through various technologies, including thermal, optical, and radar sensors, used within advanced soil hydrology models. Data were sourced from the ERA5-Land reanalysis project, which provides freely accessible global datasets at hourly temporal resolution on a 9 × 9 km spatial grid [25]. Given the relatively small size of the structure compared to the grid, a single time history was extracted for each quantity, represented in Fig. 4.

Displacement and environmental data were preprocessed before use. First, displacement data were interpolated daily. Then, the vertical component of the LOS displacements was estimated using the following equation [26]:

$$\hat{d}(\mathrm{PS}_j, t) = \frac{d_{\mathrm{LOS}}(\mathrm{PS}_j, t)}{\cos\beta} \tag{1}$$

where $d_{\mathrm{LOS}}(\mathrm{PS}_j, t)$ represents the displacement of the LOS measured at time t for the jth PS, and β denotes the incidence angle of the LOS of the satellite (i.e., $\beta = 36.4°$ for track 117-IW1 and $\beta = 45.6°$ for track 15-IW3). This simple approach mitigates the scaling differences caused by the different satellite tracks and sub-swaths.

According to the data documentation, most acquisitions occurred around 5:00 PM; therefore, all displacement measurements were assumed to correspond to this time, with a daily sampling frequency. To ensure temporal consistency, the environmental data were downsampled to the same time grid as the displacement data by extracting daily values at 5:00 PM.

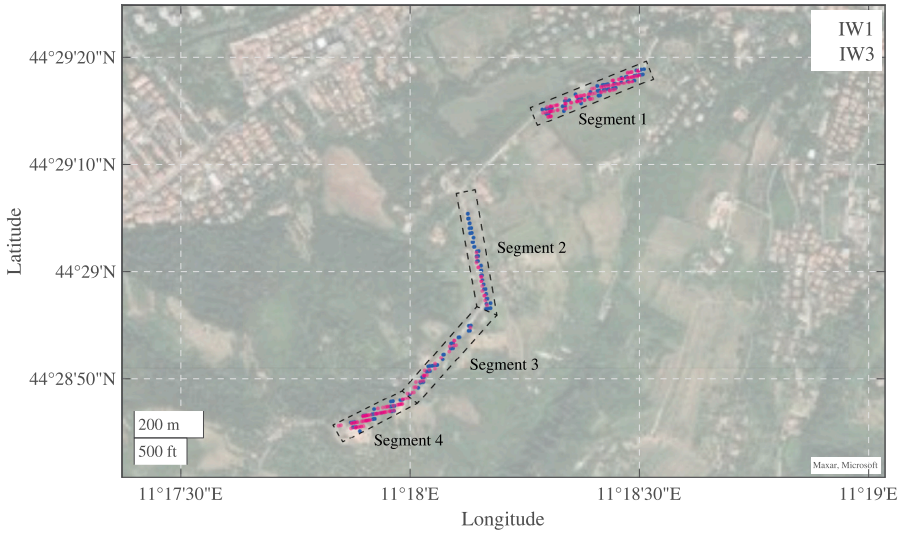

Fig. 3. Persistent scatterers (PSs) of the displacement data for the 2019–2023 interval (tracks 117-IW1 and 15-IW3).

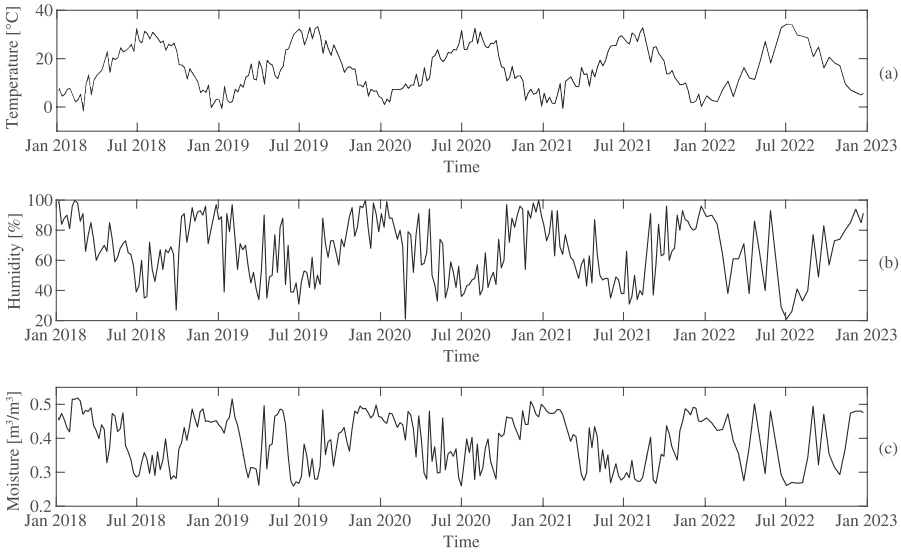

Fig. 4. Environmental driver measurements in the area of the monitored structure: (a) air temperature at 2 m above ground level, (b) air humidity at 2 m above ground level, and (c) soil moisture in the upper 7 cm of the soil.

As a result, two displacement datasets (one for each satellite track) and a single environmental dataset, all sampled at the same time instants, were generated for each structural segment.

4. Parametric structural model

A simplified numerical model of the structure was developed with two main objectives: (1) testing the SHM methodology proposed in Section 5 using simulated anomalies and (2) characterizing real anomalous data using a classifier trained on synthetic data.

The proposed model is specifically developed considering its subsequent use within the transfer learning methodologies described in Section 5.2. Thus, it captures the primary physical mechanisms that drive vertical displacements without requiring detailed information on structural or material properties [27]. Following its formulation (Section 4.1), the model parameters linking structural displacements to environmental inputs are calibrated using real measurements from the specific case study (Section 4.2). Finally, controlled damage conditions are simulated (Section 4.3).

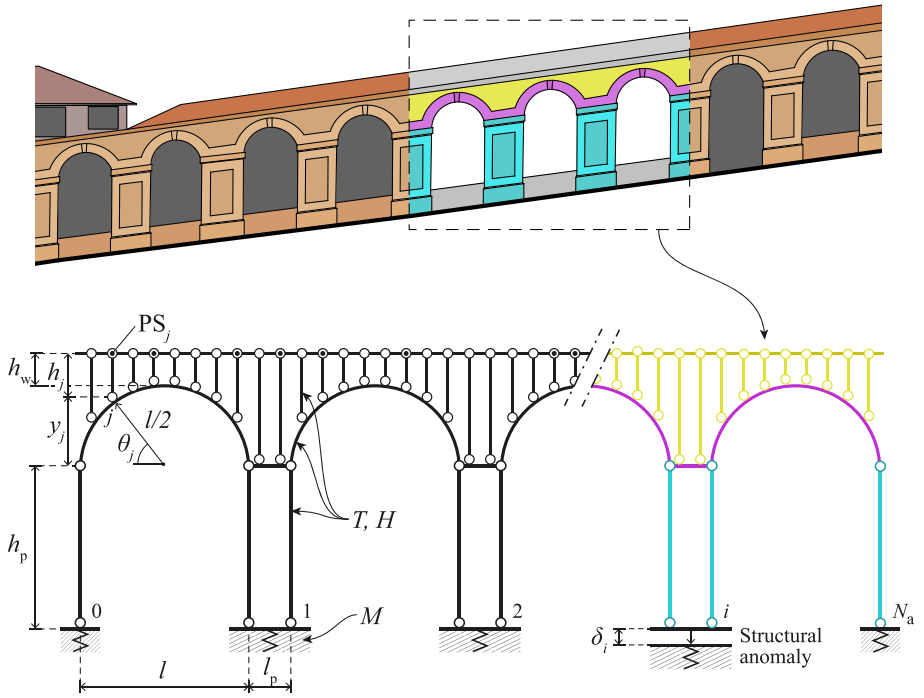

Fig. 5. Scheme of the parametric structural model used in the presented case study.

4.1. Model construction

The proposed model assumes that the displacements of PSs identified by satellites are primarily influenced by the behavior of the longitudinal arcades that supports the roof. This structure is considered identical on both sides, despite the presence of filled arches with walls on one side (see Fig. 1).

The simplified scheme of a single arcade used in this study is shown in Fig. 5. In this model, the pillars are represented as vertical truss elements. To account for their finite thickness, each pillar is modeled using two vertical truss members connected at the top by a horizontal link. The two vertical elements of each pillar are constrained to experience identical vertical displacements, thereby preventing relative rotation or deformation. The pillars support slender semicircular arches that, in turn, sustain a series of truss elements representing wall fillings, which provide support for the roof at a uniform level.

Although the mechanical behavior of masonry structures is inherently nonlinear, anisotropic, and governed by the interaction between compression, cracking, and joint behavior, the present model intentionally adopts a simplified representation. This formulation aims to capture the first-order response of the system to environmental loading while acknowledging the uncertainties inherent in satellite-derived displacement measurements. Accordingly, the model should be regarded as a reduced-order approximation capable of reproducing the dominant kinematic trends rather than the full nonlinear response of the masonry arcade.

For this study, the following parameters were set, with reference to Fig. 5, based on approximate measurements of the analyzed structure: $h_p = 4.5\,\text{m}$, $l = 3\,\text{m}$, $h_w = 0.5\,\text{m}$, and $l_p = 1.7\,\text{m}$.

The effects of environmental drivers, such as temperature and humidity, on porous materials (e.g., masonry bricks and mortar) have been extensively studied, with various models developed to characterize adsorption/desorption isotherms, induced strain states, and their impact on long-term material expansion and durability [28–34]. In this study, these complex interactions are not explicitly modeled. Instead, their effects are represented through a simplified linear regression, using approximated geometrical parameters and calibrated coefficients tuned to reflect observed trends.

Pillars and wall-filling elements are modeled as infinitely stiff components that only expand (or contract) axially in response to air temperature and humidity. The vertical displacement of the pillars (d_p) and the wall filling elements (d_w), is expressed as follows:

$$d_p(t) = \alpha_T h_p T(t) + \alpha_H h_p H(t - \tau_H) \tag{2a}$$

$$d_w(h_j, t) = \alpha_T h_j T(t) + \alpha_H h_j H(t - \tau_H) \tag{2b}$$

where t is a discrete time index, h_p and h_j denote the height of the pillars and of the jth beam in the wall filling model, while $T(t)$ and $H(t)$ correspond to air temperature and percentage humidity over time, respectively. Here, α_T and α_H represent an equivalent

linearized thermal expansion coefficient of the general material and an analogous linear coefficient that accounts for humidity-induced expansion, respectively. Furthermore, τ_H is a time delay parameter that accounts for the delay between the measured humidity driver and its effect on the structure. Due to the long sampling period of satellite displacement data, thermal inertia is not considered, as it is mainly due to daily temperature cycles.

In this model, the arches deform exclusively due to environmental effects and horizontal thrust. Specifically, both temperature and humidity are assumed to cause elongation of the arch axis in the form of uniform thermal deformation. Given the modular nature of the structure, each pillar can be considered along a symmetry axis. As a result, arches are constrained to vertical displacements, expressed as:

$$d_a(\theta_j, t) = \left(\alpha_T T(t) + \alpha_H H(t - \tau_H)\right)\left(\pi l \sin^2 \theta_j + y_j\right) \tag{3}$$

where θ_j is the angle formed by the jth point of the arch with the springing point, and, and $y_j(\theta_j)$ is the vertical coordinate of this point relative to the impost.

Air temperature and humidity were selected as the most significant environmental drivers for masonry components, according to studies in the literature [2]. In this model, pillars, arches, and wall fillings all contribute to displacements at the roof level.

In addition, soil moisture was considered an environmental factor influencing soil properties. While the response of soft soils (such as those in the studied area [35]) is governed by complex interactions affecting shear strength, cohesion, and compressibility [36,37], a simplified representation is adopted here. The soil is modeled using a Winkler-type foundation, idealized as an elastic bed of springs whose stiffness varies with the soil moisture level. The base displacement of each pillar due to the effective weight of the structure W applied on a time-varying elastic soil can be expressed as:

$$d_s(t) = \frac{W}{k_M(t - \tau_M)} \tag{4}$$

where k_M is the soil stiffness function of t and τ_M, which is a lag parameter. Since k_M is assumed to vary inversely with the moisture content ($M(t)$), the relation can be conveniently reformulated in an equivalent linearized form as:

$$d_s(t) = \alpha_M M(t - \tau_M) \tag{5}$$

where α_M is an empirical coefficient combining the effects of weight and soil stiffness. This formulation represents a first-order correlation between the structural displacement and the measured soil moisture variations, sufficient for capturing the environmental contribution within the considered time scale.

To generate displacement time histories compatible with satellite observations, PSs are randomly selected from the top points of the model (see Fig. 5), with the total number specified by the user. The selected displacements are influenced by air temperature, humidity, and soil moisture, following the physical models described above, and are expressed as:

$$d(\mathrm{PS}_j, t) = d_p(t) + d_w(h_j, t) + d_a(\theta_j, t) + d_s(t) + \epsilon(t) \tag{6}$$

Notably, a noise term $\epsilon(t)$ is included, modeled as a Gaussian process with zero mean and standard deviation σ_ϵ.

4.2. Model calibration

Once the geometric parameters of the model (l, l_p, h_p, h_w, and the number of arches N_a) are defined to match the selected case study, the environmental driver parameters must be calibrated. These include α_T, α_H, α_M, the time lags τ_H and τ_M, and the standard deviation of the noise σ_ϵ. The calibration is performed through a two-step optimization process.

First, for a given number of iterations or until a specified error tolerance is reached, the mean displacement across all PSs within a given time interval is compared to the mean displacement observed in real data at the corresponding time samples. In this step, the noise standard deviation is set to zero. At each iteration, the parameters are adjusted, and the discrepancy between simulated ($\mu_s(t)$) and observed ($\mu_r(t)$) mean displacements is quantified. To this aim, the root mean square error (RMSE) was used to define a cost function (J) as follows:

$$J(\alpha_T, \alpha_H, \alpha_M, \tau_H, \tau_M) = \sqrt{\frac{1}{t_{tot}} \sum_{t=1}^{t_{tot}} \left(\mu_s(t) - \mu_r(t)\right)^2} \tag{7}$$

with:

$$\mu_s(t) = \frac{1}{N_s} \sum_{j=1}^{N_s} d(\mathrm{PS}_j, t) \tag{8a}$$

$$\mu_r(t) = \frac{1}{N_r} \sum_{j=1}^{N_r} \hat{d}(\mathrm{PS}_j, t) \tag{8b}$$

Here, t_{tot} is the total number of time samples available for real displacement measurements $\hat{d}(\mathrm{PS}_j, t)$, while N_s and N_r denote the number of PSs used in the simulation and those available in the real dataset, respectively, which may differ. Any linear trend (such as a uniform movement affecting the entire monitored area) is removed from $\mu_r(t)$ before fitting. Thus, in Eq. (8b), $\mu_r(t)$ represents mean displacements with the linear trend removed.

Table 1
Calibrated parameters of the simulated segments.

Segment	α_T [°C^{-1}]	α_H [−]	α_M [mm]	τ_H [days]	τ_M [days]	N_a	RMSE [mm]
1 117-IW1	2.89×10^{-5}	5.30×10^{-5}	−68.4	90	90	62	4.3
2 117-IW1	3.36×10^{-5}	5.30×10^{-5}	−57.9	10	10	61	4.4
3 117-IW1	4.31×10^{-5}	5.30×10^{-5}	−57.9	40	40	71	4.3
4 117-IW1	5.26×10^{-5}	5.30×10^{-5}	−57.9	40	40	33	4.3
1 15-IW3	3.84×10^{-5}	5.30×10^{-5}	−68.4	80	80	62	3.8
2 15-IW3	2.42×10^{-5}	5.30×10^{-5}	−78.9	30	30	61	4.8
3 15-IW3	1.94×10^{-5}	5.30×10^{-5}	−68.4	90	90	71	4.3
4 15-IW3	2.89×10^{-5}	5.30×10^{-5}	−68.4	90	90	33	4.4

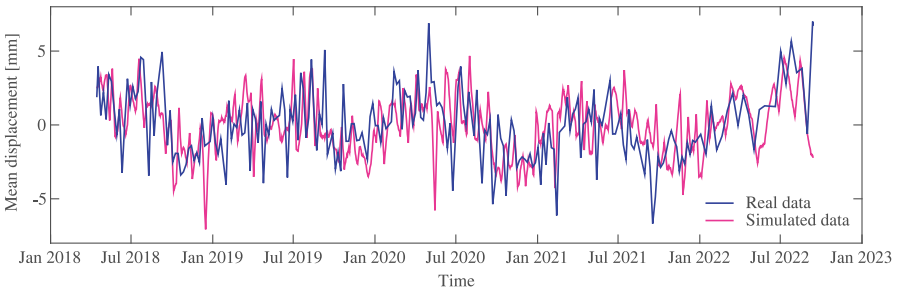

Fig. 6. Comparison between the detrended mean of real displacements (segment 1 117-IW1) and the mean of displacements provided by the calibrated model.

Since the model includes the lag parameters τ_H and τ_M, a systematic search over predefined parameter ranges was performed to identify the global minimum of the cost function and to avoid convergence to local minima that may arise from the non-convexity induced by the lag terms. Specifically, the following ranges were used for each parameter: $\alpha_T = [10^{-5}, 10^{-4}]\,°C^{-1}$, $\alpha_H = [-10^{-1}, 10^{-1}]$, $\alpha_M = [-10^2, 10^2]$ mm, each discretized into 20 equally spaced values. Furthermore, positive lags up to 100 days, discretized every 10 days, were tested for τ_H and τ_M, separately.

Since environmental drivers are not measured directly on site but estimated through complex hydrogeologic models [25], they involve multiple inputs beyond the three primary drivers considered here. Therefore, the coefficients (and lags) used in this model should not be interpreted solely as relating to the relevant drivers; instead, they should be seen as global coefficients that account for multiple underlying phenomena with the general aim of minimizing the difference between modeled and measured displacements.

The second step of the optimization process focuses on determining the noise level in the simulated displacements. In this study, the noise parameter σ_ϵ is set to 2.5 mm, ensuring a 97% probability that the measured displacement lies within ±5 mm of the true value. This level was found to produce statistical characteristics consistent with those observed in the real displacement data.

Eight synthetic structural segments were generated to replicate the data of the four real segments described in Section 3, with each satellite track considered separately. Table 1 presents the parameters obtained through calibration, selecting the global minimum of the cost function described in Eq. (7). The table also includes the number of arches N_a for each simulated model and the RMSE of the final mean displacement (before noise was added). A total of 100 PSs were extracted from each simulated segment.

Notably, in all cases, $\tau_H = \tau_M$, indicating a correlation between the two. Moreover, the optimal α_H was consistent in all segments.

An example of the optimization result is shown in Fig. 6 for segment 1 117-IW1, comparing the detrended mean displacement of all real PSs with that of simulated PSs over the analyzed period. The figure demonstrates that the simulated displacement closely follows the trend observed in the real data (with an RMSE of 4.3 mm, as summarized in Table 1), confirming the effectiveness of the simplified linearized model in capturing the structural response to environmental drivers.

4.3. Simulated anomaly scenarios

Once the model parameters are calibrated, anomaly scenarios can be simulated to replicate expected anomalies that may impact the observed vertical displacements. This study considers two types of structural anomalies: settlements and uplifts, which affect different portions of the structure to varying extents. Table 2 summarizes the simulated anomaly scenarios that will be used later to train a classifier. The intensity parameter represents the average displacement imposed at the base of consecutive pillars in the affected structural portions. Fig. 7 illustrates these concepts, showing examples of settlement and uplift scenarios as well as the superposition of time-dependent environmental effects.

5. Proposed SHM methodology

The proposed SHM procedure involves the following steps: (1) extracting features sensitive to structural anomalies from satellite displacement data for each segment of the structure, (2) harmonizing these features through domain adaptation to eliminate

Table 2
Anomaly types considered in the study with corresponding intensities.

Anomaly type	Description	Intensity
1	Settlement of 1/10 of the pillars in the segment	5 mm 10 mm 15 mm
2	Settlement of 1/5 of the pillars in the segment	5 mm 10 mm 15 mm
3	Uplift of 1/10 of the pillars in the segment	5 mm 10 mm 15 mm

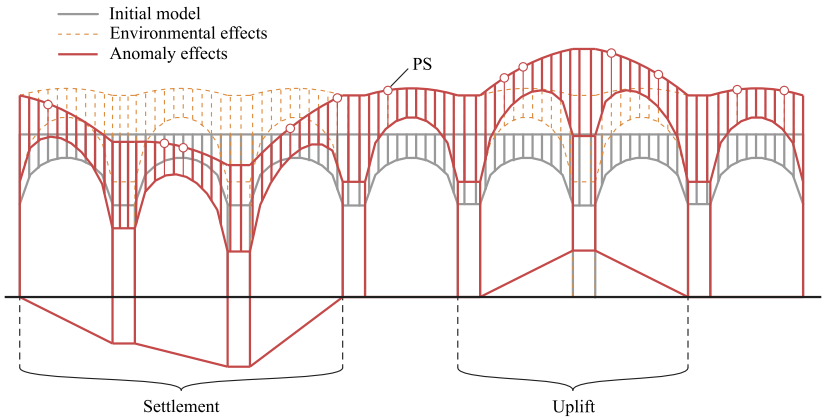

Fig. 7. Example of the effects of environmental drivers and different anomaly configurations on the proposed model.

segment-specific characteristics that are not related to structural conditions, (3) defining an anomaly detection criterion based on direct comparisons between segments, and (4) characterizing detected anomalies using synthetic labels derived from the simplified parametric model.

Fig. 8 summarizes the methodology described above, which is further detailed in the following.

5.1. Feature extraction

The locations of PSs extracted from InSAR imagery are affected by geolocation uncertainties arising from the displacement retrieval process. In addition, individual Sentinel-1 displacement time series have moderate single-epoch accuracy. To mitigate these limitations, the proposed analysis relies on the statistical characterization of displacement data rather than attempting a one-to-one correspondence between PSs and specific structural elements. Interpreting InSAR measurements through aggregated statistical descriptors minimizes the impact of PS positional uncertainty, reduces sensitivity to noise in individual time histories, and ensures consistent parameter extraction across all structural segments.

Previous research on bridges has demonstrated that statistical moments can effectively capture structural anomalies, such as settlements and uplifts, as well as data anomalies (e.g., outliers) [15]. Building on these findings, the present study adopts the same set of statistical features, listed in Table 3, computed from the satellite-based displacement time histories. Each feature is evaluated at every time instance; for example, f_1 corresponds to the mean displacement of all PSs within a given structural segment, while f_2 represents the standard deviation of the displacement values at the same time. Additional statistical descriptors are computed in an analogous manner for the remaining features.

5.2. Feature harmonization

Due to potential variations in segment geometry and orientation, features extracted from different segments may exhibit different trends, making direct comparison and detection of anomalous segments challenging.

To address this issue, SA is used as a domain adaptation technique. SA is designed to align the feature spaces of distinct domains (referred to as a “source” domain and multiple “target” domains) by reducing the differences in their marginal distributions [38]. This method operates under the assumption that, while the source and target domains may exhibit distributional differences, they share an underlying latent structure. By projecting data from both domains onto a common subspace, SA enables cross-domain analysis.

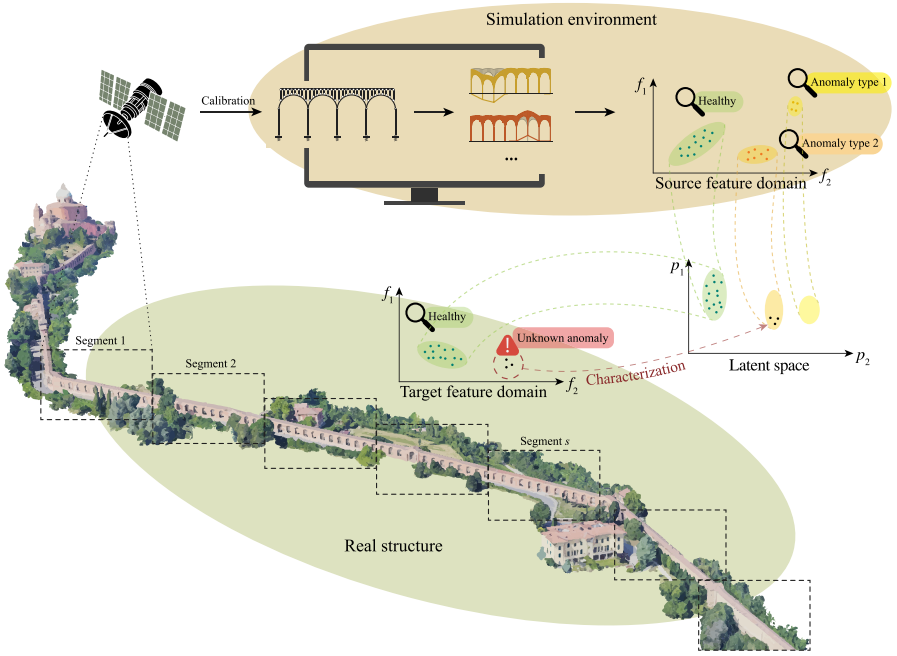

Fig. 8. Workflow of the proposed methodology. The structural segments shown here are for demonstration purposes and do not correspond to those used in the analyses.

Table 3
Set of selected statistical features for each segment.

Feature	Description
f_1	Mean value of the instantaneous vertical displacements
f_2	Standard deviation of the instantaneous vertical displacements
f_3	Distribution skewness of the instantaneous vertical displacements
f_4	Distribution kurtosis of the instantaneous vertical displacements
f_5	Minimum value of the instantaneous vertical displacements
f_6	Maximum value of the instantaneous vertical displacements
f_7	Median of the instantaneous vertical displacements
f_8	Vertical displacement component with maximum variance over the analyzed interval

In this framework, a selected structural segment serves as the reference (source domain) for constructing the aligned subspace into which the features of all target segments are projected. Typically, the reference segment is chosen based on the availability of more detailed information about the structure, such as known labels indicating anomalous conditions or its simplicity in inspection. This facilitates knowledge transfer to all target segments. Further clarification on this concept is provided in Section 5.4.

Let $\mathbf{F}^{(s)} \in \mathbb{R}^{D\times K}$ represent the feature matrix for structural segment s, which collects D instances of the features listed in Table 3 (one for each column of this matrix). Here, D is the number of instances in a "baseline" interval (i.e., the time span of the dataset), while K denotes the number of extracted features (in this case, 8). Without loss of generality, segment 1 is designated as the source domain.

The first step involves mean-centering each column of $\mathbf{F}^{(s)}$ and normalization such that it has a unitary standard deviation. It is important to note that the mean and standard deviation values used to normalize this baseline dataset will also be used to normalize future data.

Then, principal component analysis (PCA) is applied to extract the top $r \leq K$ principal vectors from each domain, corresponding to the r largest eigenvalues. These vectors, collected in $\mathbf{V}^{(s)} \in \mathbb{R}^{K\times r}$, serve as the basis for the subspace of each domain. Specifically, $\mathbf{V}^{(1)} \in \mathbb{R}^{K\times r}$ defines the source subspace, while $\mathbf{V}^{(s)} \in \mathbb{R}^{K\times r}$ represents the target subspaces for each segment $s \neq 1$.

To align the target data with the source subspace, a projection matrix is computed as follows:

$$\mathbf{W}^{(s)} = \mathbf{V}^{(s)}\mathbf{V}^{(s)\top}\mathbf{V}^{(1)} \tag{9}$$

This matrix enables the transformation of the target subspace into the coordinate system of the source subspace by aligning their basis vectors. Consequently, the source and target baseline data projected onto this common "latent" space are given by:

$$\mathbf{P}^{(1)} = \mathbf{F}^{(1)}\mathbf{V}^{(1)} \tag{10a}$$

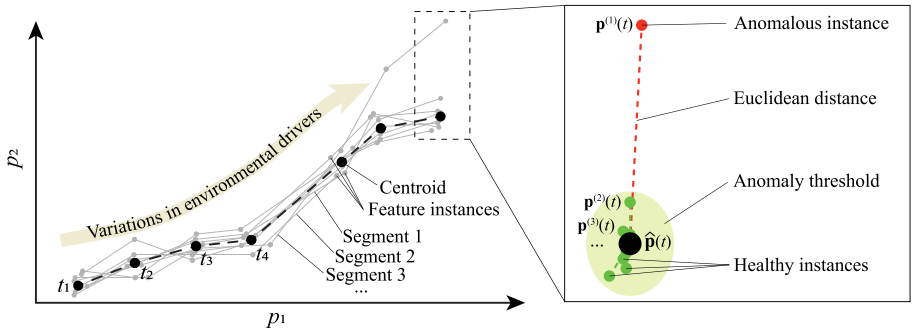

Fig. 9. Proposed approach for anomaly detection.

$$\mathbf{P}^{(s)} = \mathbf{F}^{(s)}\mathbf{W}^{(s)} \tag{10b}$$

These equations can also be used to project future data instances $\mathbf{f}^{(s)}(t) \in \mathbb{R}^{1\times K}$ (i.e., obtained at instant $t > D$) onto the latent space, as follows:

$$\mathbf{p}^{(1)}(t) = \mathbf{f}^{(1)}(t)\mathbf{V}^{(1)} \tag{11a}$$

$$\mathbf{p}^{(s)}(t) = \mathbf{f}^{(s)}(t)\mathbf{W}^{(s)} \tag{11b}$$

Here, vectors $\mathbf{f}^{(s)}(t)$ and $\mathbf{p}^{(s)}(t)$ have the same structures as the rows of the matrices $\mathbf{F}^{(s)}$ and $\mathbf{P}^{(s)}$, respectively.

In this study, r is set equal to K since dimensionality reduction is not the objective of the proposed approach.

Given the similarities in segment configurations and environmental conditions, the principal components and transformation matrices derived for each structure are expected to be consistent across all segments.

5.3. Anomaly detection

Under healthy conditions, the features of different segments within the same structure should exhibit similar variations in the latent space, when influenced by time-dependent environmental factors. However, when structural anomalies occur, the underlying physics of the affected segments change, altering the relationships between features. Consequently, data from "anomalous" (or "damaged") structural segments will deviate from the expected patterns observed in the rest of the structure. Furthermore, if multiple segments experience the same anomaly, their features will cluster within the same region of the latent space.

Building on this principle, Quqa et al. [15] introduced a damage index based on the Euclidean distance of each feature instance from the instantaneous centroid of all monitored segments (i.e., the mean of each instantaneous feature across all structures in the monitored population at a given time). The centroid is expected to follow a trajectory representing the overall behavior of the structure in the feature space (which will approximate the healthy behavior if the anomaly affects a limited subset of the population). An anomaly threshold can then be defined as the maximum distance of each individual in the population from the centroid, and any feature instance beyond this threshold is considered indicative of an anomaly. This concept is illustrated in Fig. 9 in a two-dimensional projection of the latent space (i.e., $p_1 - p_2$).

Including noisy or anomalous data in the centroid calculation may bias the centroid itself, shifting it away from the true healthy condition and leading to incorrect identification of anomalies during the detection process. To address this issue, this study proposes an improved approach in which the centroid position is predicted based on historical feature measures using an autoregressive model with exogenous inputs (ARX):

$$\hat{\mathbf{p}}(t) = \sum_{i=1}^{N} \hat{\mathbf{p}}(t-i)\mathbf{A}_i + \sum_{j=1}^{M} \mathbf{u}(t-j)\mathbf{B}_j + \mathbf{e}(t) \tag{12}$$

Here, $\hat{\mathbf{p}}(t) \in \mathbb{R}^{1\times r}$ represents the position of the centroid, while $\mathbf{u}(t) = [T(t), H(t-\tau_{\mathrm{H}}), M(t-\tau_{\mathrm{M}})] \in \mathbb{R}^{1\times 3}$ is the vector of environmental drivers. The matrices $\mathbf{A}_i \in \mathbb{R}^{r\times r}$ and $\mathbf{B}_j \in \mathbb{R}^{3\times r}$ are the corresponding coefficient matrices, while N and M denote the number of past time instances considered in the model for the past feature data and exogenous inputs, respectively (i.e., the orders of the model, here selected as $N = M = 10$). Finally, $\mathbf{e}(t)$ represents the residual error.

This model is initially trained to determine the optimal coefficients of the matrices $\mathbf{A}_i$ and $\mathbf{B}_j$ using a baseline data interval (specifically, 30% of the analyzed time period), assuming that all segments are non-anomalous. This baseline period can also coincide with the interval used to define the SA projection matrices. During training, the centroid is calculated as the mean of each feature across all segments. Once trained, the model can predict the centroid position for unseen feature data.

By learning the relationship between past features and environmental drivers, this model offers a more robust estimate of $\hat{\mathbf{p}}(t)$, which mitigates the variability of the centroid due to the changing environment and outliers in the individual features.

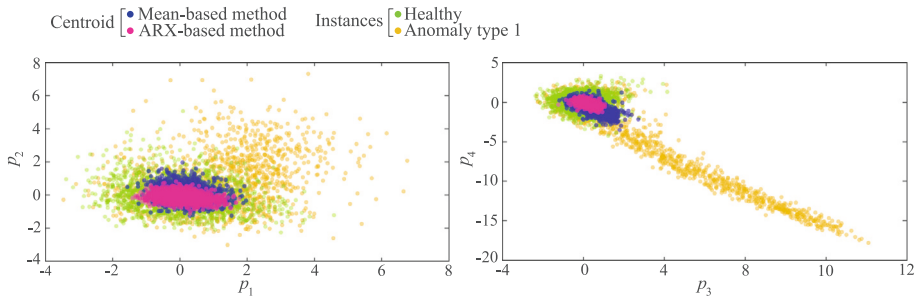

Fig. 10. Comparison of two methods for centroid prediction during a growing-intensity anomaly. The figures show two two-dimensional projections of the latent space.

Fig. 10 compares the centroid positions obtained using the mean-based approach and those predicted by the ARX model. In this example, green points represent healthy data for synthetic segment 1 117–IW1 within a selected time interval, while yellow points represent the same segment subjected to a progressive type-1 anomaly (settlement increasing from 0 to 20 mm) over the same interval. The centroids are computed considering all eight modeled segments when 1 117-IW1 is anomalous and all the others are healthy. The centroids derived from the mean-based approach (blue points) are more dispersed and more strongly influenced by the anomaly, whereas the ARX-based predictions (magenta points) remain compact and aligned with the healthy region. This directly affects the computation of the damage index, as discussed in the following section.

The damage (or anomaly) index (DI) for each structural segment is defined as the Euclidean distance at time t between the feature vector of segment s and the estimated centroid:

$$\mathrm{DI}_s(t) = \|\mathbf{p}^{(s)}(t) - \hat{\mathbf{p}}(t)\| \tag{13}$$

Fig. 11 shows the DI evaluated for three simulations. Each simulation involves monitoring the 8 synthetic structural segments calibrated as explained in Section 4.2. In each simulation, a different anomaly type is imposed on one single segment starting on December 5, 2019, with an intensity that increases linearly over time up to 20 mm by December 25, 2022. The three anomaly types used in the three simulations are those described in Table 2.

In each simulation, the DI is calculated using Eq. (13), where s denotes the index of the anomalous segment. For comparison purposes, the centroid position $\hat{\mathbf{p}}(t)$ was estimated using both the ARX-based and the mean-based methods, producing two corresponding DI curves, shown in Fig. 11 in black and orange, respectively. A threshold for damage detection (green dashed line) was defined to achieve a false positive rate (FPR) of 1% within the baseline interval for the ARX-based DI (gray-shaded region). This threshold can be adjusted by the user depending on the acceptable false-alarm rate.

The resulting DI increases nearly proportionally with the simulated anomaly intensity in all cases. The DI computed using the ARX-based method shows slightly higher sensitivity to damage, as indicated by larger deviations beyond the anomaly threshold with respect to the mean-based DI. This improvement arises because mean-based centroids are more influenced by transient anomalies in individual segments, whereas the ARX-based centroids maintain greater stability within the feature space (see Fig. 10). Nevertheless, due to measurement noise, anomalies with amplitudes below approximately 5 mm remain below the detection threshold and are typically indistinguishable from background variability.

5.4. Anomaly characterization

The rationale behind the anomaly characterization procedure proposed in this study is that, by projecting the features of different segments onto a common latent space, the same changes in structural behavior will shift the feature instances in the same direction for all harmonized segments. As a result, different anomaly types will define distinct regions in the latent space. For instance, Fig. 12 illustrates the anomalies listed in Table 2 imposed on synthetic segment 1 117-IW1, shown in two different views of the latent space.

Thus, labels can be assigned to different regions of the latent space based on damage scenarios modeled through the proposed simplified model, as shown in Fig. 12. The characterization of anomalous feature instances is then performed by examining the regions of the latent space populated by each feature instance.

The anomaly classification method proposed in this study relies on the k-Nearest Neighbors (KNN) algorithm, a widely used machine learning technique for classification tasks [39]. KNN is a non-parametric, instance-based learning method that classifies new data points by examining the majority class of their nearest neighbors in the feature space. The algorithm works by calculating the distance between an unseen data point and all existing labeled data points, selecting the k closest neighbors (in this paper, $k = 25$), and assigning a class label based on the majority vote.

The labeled datasets used in the KNN process were generated from simulated data instances under the anomaly scenarios detailed in Table 2. To evaluate the reliability of the classification procedure, 100 unseen data instances were generated using segment 1 117-IW1 under each simulated damage condition. These instances were then classified using the trained KNN model, and the results

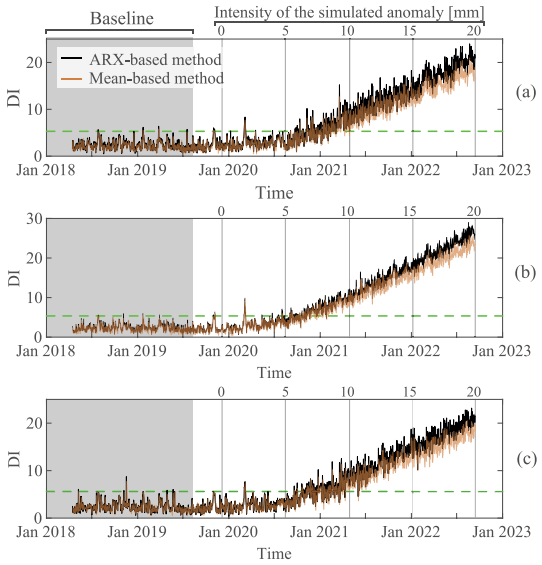

Fig. 11. Damage index evaluated for the simulated segments during linearly increasing anomaly intensity: (a) simulation 1 (anomaly type 1), (b) simulation 2 (anomaly type 2), (c) simulation 3 (anomaly type 3). The green dashed line indicates the anomaly threshold.

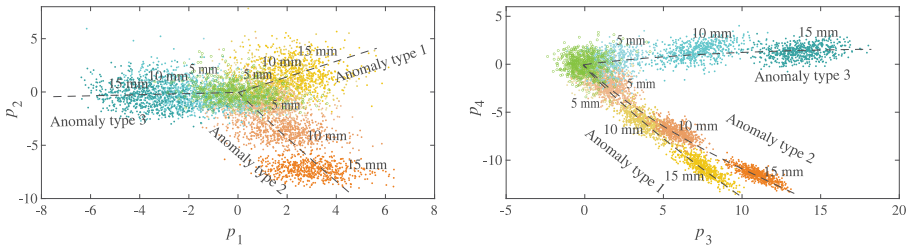

Fig. 12. Feature distributions of simulated anomaly types.

are presented in the confusion matrix shown in Fig. 13. Here, the true positive rate (TPR), false negative rate (FNR), precision, and false discovery rate (FDR) are reported for each class as performance indicators.

The classification outcomes are consistent with those obtained for damage detection: scenarios with small damage amplitudes (5 mm) are frequently misclassified, indicating a lower detection confidence.

Furthermore, Fig. 14 illustrates the anomaly classification results obtained using the KNN model for the simulations shown in Fig. 11. In the figure, the varying circle sizes represent the intensity of the anomalies in the assigned labels, while the annotations at the top of the figure indicate the actual simulated anomaly intensity. The circles representing classification outcomes are partially transparent in the figure, with persistent anomalies (and thus overlapping circles) resulting in a more solid color. Only the data identified as anomalous in Fig. 11 (i.e., those exceeding the anomaly threshold) have been classified. Additionally, some over-threshold data points were classified as "healthy", indicated by small black dots in the figure.

The classifier successfully assigned the correct labels to most anomalies above the threshold, with intensities increasing over time. Consistent with the confusion matrix results, the method demonstrates reliable performance for anomalies with amplitudes exceeding approximately 5–6 mm, which suggests a threshold for anomaly significance.

6. Application to the real structure

This section presents the results obtained by applying the proposed methodology to the real segments of the Portico di San Luca described in Section 3. The two datasets from tracks 117-IW1 and 15-IW3 are used independently, resulting in a total of 8 structural segments for the analysis.

First, features are extracted from the displacement data following the procedure outlined in Section 5.1. The features obtained during the interval from April 15, 2018, to December 5, 2019 (600 instances, approximately 30% of the available dataset) are used to construct the projection matrices $\mathbf{W}^{(s)}$, as described in Section 5.2, assuming that all segments of the structure are "healthy" during this period. Notably, the source domain still consists of the synthetic structure calibrated on segment 1 117-IW1, which is

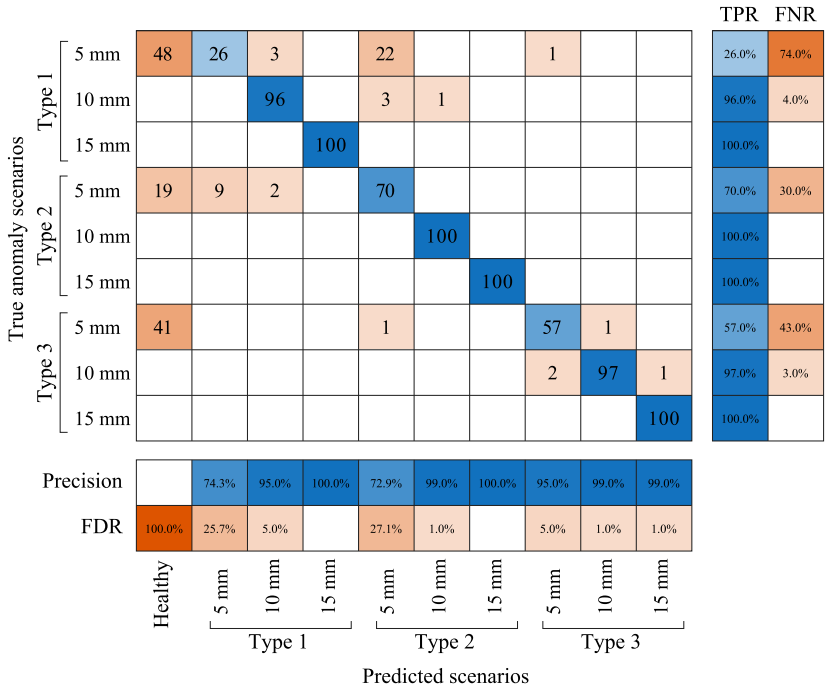

Fig. 13. Confusion matrix obtained from simulated unseen data samples.

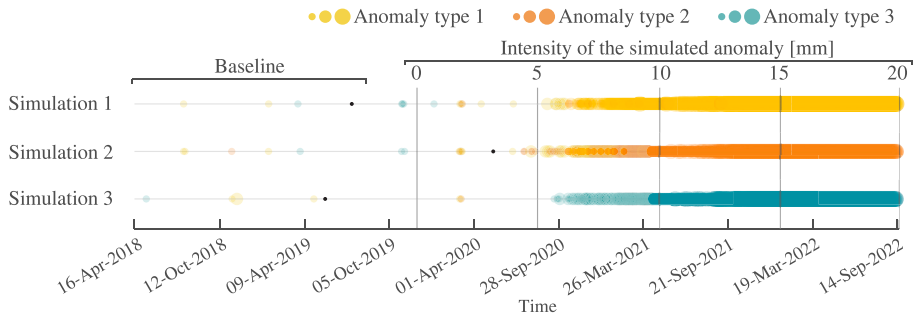

Fig. 14. Classification results for the simulated scenarios.

used to construct the projection matrix $\mathbf{V}^{(1)}$ for the same time interval. In this way, synthetic damage simulated in the source domain will be used to characterize anomalous feature instances found in the target domain (i.e., the real structure).

The entire real dataset is then projected onto the latent space (Eq. (11a)), where the DI is calculated for each individual segment, as explained in Section 5.3. The results obtained are shown in Fig. 15, where the green line represents the anomaly threshold, set at the mean of the DI within the baseline interval plus 3 standard deviations. Notably, the DI measures the relative behavior of each segment in comparison to the overall trend (i.e., the centroid trajectory), effectively filtering out effects that impact the entire structure, such as common environmental conditions and global ground movements (see also Appendix A). Both satellite tracks for segment 1 show a consistent increase in the DI starting from mid-2020. A similar trend is observed for segment 2, beginning in early 2021, with some differences between the two satellite tracks. These differences may be attributed to the varying coverage of the PSs in the different satellite tracks. As shown in Fig. 3, the acquisition 15-IW3 covers the entire segment, while 117-IW1 only covers the southern portion. For the other segments, occasional outliers exceed the threshold without a clear trend.

Then, similar to the simulations conducted in Section 5.4, the instances found anomalous in Fig. 11 have been classified in the labels generated through the simulated model. Fig. 16 presents the classification results for the analyzed period between 2018 and 2022. In this figure, the circles on the timeline for each segment and satellite track represent the classified anomaly at each date, with their color indicating the anomaly type and their size proportional to the anomaly intensity (based on the cases used for training, see Table 2).

Anomalies in both satellite tracks of segment 1 are classified as “anomaly type 2”, corresponding to a settlement affecting 1/5 of the pillars in the segment, with the smallest simulated intensity. Although these anomalies are not uniformly observed over time (as

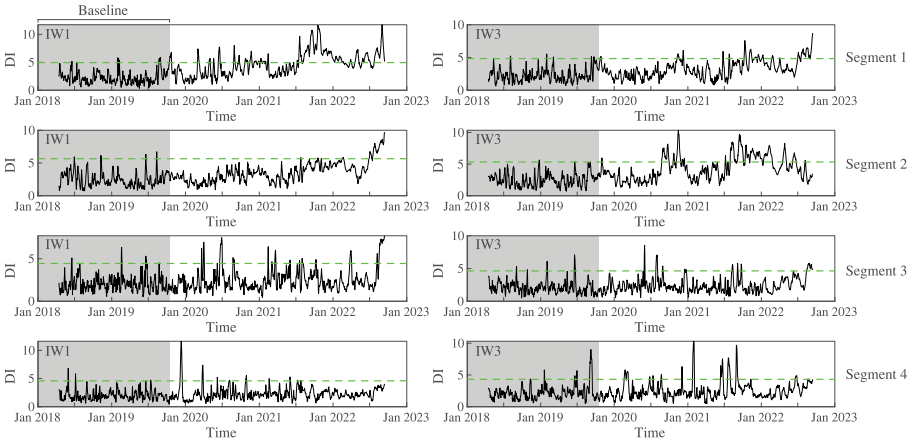

Fig. 15. Damage index evaluated for the monitored segments during the 2018–2022 interval.

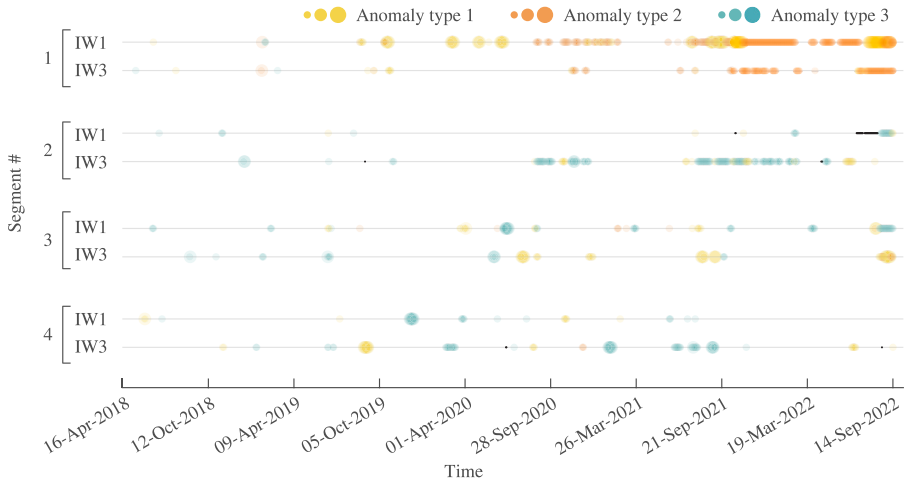

Fig. 16. Classification results for the 2018–2022 interval.

seen in the early anomaly cases shown in Fig. 14), a noticeable increase in their occurrence is observed at the end of 2021 for track 117-IW1. Previous evaluation campaigns reported rising damp within the masonry between Mysteries III and V and considerable plaster detachment in both the arch structures and vaults (see Fig. 17(a)).

A plausible interpretation is that localized settlements may have induced microcracking in the masonry, facilitating capillary water rise and moisture accumulation. Conversely, water saturation can lead to a progressive reduction in the load-bearing capacity of the masonry, while salt crystallization cycles can alter the pore structure, exacerbating material degradation [40]. The concurrent occurrence of settlement and rising damp therefore suggests coupled hydro-mechanical processes that modify the structural behavior and are reflected in the observed increase of the damage index. Extensive restoration works recently carried out along the Portico further confirm the need for maintenance interventions in this area.

This result is further supported by the average velocity map in Fig. 18, which shows the average velocity of movement for each PS calculated throughout the analyzed time interval.

The regions of segment 2 exhibiting high DI values were predominantly classified as uplifts affecting approximately 1/10 of the pillars. Since this anomaly was detected only in track 15-IW3, it is likely confined to the northern portion of the segment, which is exclusively covered by 15-IW3, as confirmed by the velocity map in Fig. 18. The DI did not remain consistently above the threshold over time, and several over-threshold instances were not successfully classified (as indicated by the black dots in the later part of track 117-IW1). This behavior suggests either a low anomaly intensity or the need to extend the range of simulated scenarios for improved characterization. It is also worth noting that a structural disconnection was introduced in the past between segments IX and X, which may explain the different movements observed in this area (Fig. 17(b)).

Outliers detected in the remaining segments appear as isolated points with inconsistent classifications and no clear temporal persistence. This pattern suggests that they likely correspond to noise-induced artifacts or transient physical phenomena not represented in the simplified model adopted in this study, rather than to permanent damage conditions. This interpretation is

Fig. 17. Pictures of structural details: (a) efflorescence caused by rising damp between Mysteries IV and V, documented in 2020, (b) structural disconnection between Mysteries IX and X, documented in 2025.

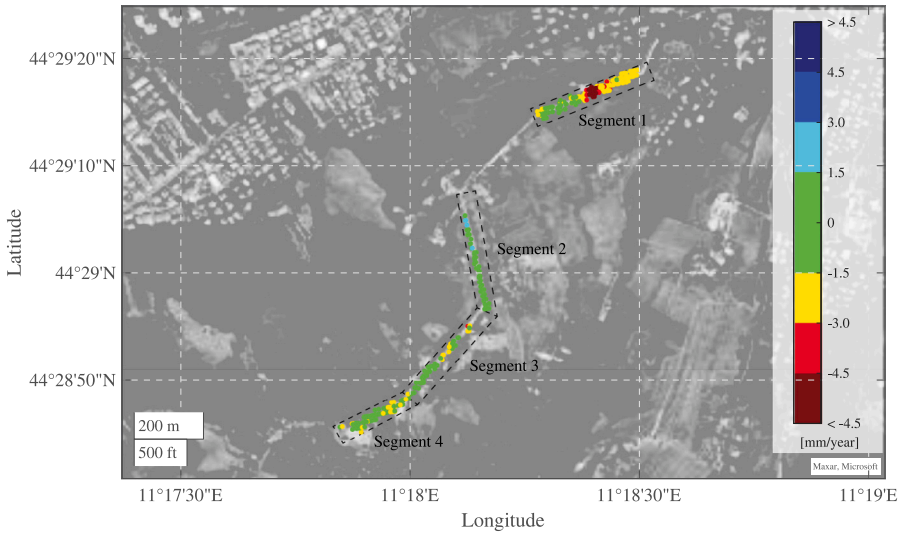

Fig. 18. Average yearly velocity map for the 2018–2022 interval (aggregated from all satellite tracks).

consistent with findings from previous evaluation campaigns, which did not identify any significant structural issues in segments 3 and 4.

It is important to note that the anomalous displacements observed in this study do not necessarily correspond to purely vertical movement, as the measurements are taken along the LOS, then scaled according to the incidence angle. Therefore, "uplift" should be interpreted as a shift of the PSs towards the satellite position, while "settlements" represent movement in the opposite direction, potentially including horizontal components.

Appendix B presents the results shown in Figs. 15 and 16 for a different time interval, from 2019 to 2023, also available on the EGMS portal. Overall, the results are consistent with those discussed in this section, further supporting their validation. These results show that the intensity of the anomalies and their uniformity in time increase for segments 1 and 2, suggesting an evolving scenario.

7. Conclusions

This study presents a methodology for detecting and characterizing structural anomalies in modular historical structures using satellite-based measurements. The proposed approach combines anomaly detection through the comparison of harmonized features from different structural segments and anomaly classification based on synthetic labels derived from simplified structural models. The methodology was applied to the Portico di San Luca, a historical arcade in Bologna, Italy.

The use of a damage index defined as the distance of each segment from the overall structural behavior, combined with the application of an ARX model for its prediction, proved robust against measurement noise and environmental-induced variability.

Analysis of four Portico segments during the 2018–2022 period revealed consistent anomaly patterns across different satellite tracks, particularly in segment 1, where a clear increase in the DI was observed starting in mid-2020. This anomaly was classified as a settlement, aligning with findings from average velocity maps. The five-year data span enabled the derivation of velocity maps that effectively filtered environmental influences, facilitating direct comparison. Results from the extended 2019–2023 dataset further confirmed the robustness and reliability of the proposed approach.

The study also highlighted the limitations of the current modeling framework. The simplified structural model adopts a vertically constrained representation of the arcades that captures only the first-order kinematic effects of environmental loading. Consequently, damage mechanisms unrelated to ground-induced settlements are not represented. Moreover, the assumption of symmetry between opposite sides of the Portico neglects potential asymmetries arising from wall fillings or boundary conditions. Future developments will focus on studying more refined mechanical models and using high-resolution InSAR data.

The proposed methodology provides a valuable and scalable framework for population-based, satellite-informed structural health monitoring. Its applicability to historical modular structures demonstrates its potential as a cost-effective and non-invasive tool for the preservation and preventive maintenance of cultural heritage assets.

CRediT authorship contribution statement

Wael Alahmad: Writing – original draft, Software, Methodology, Investigation, Formal analysis, Data curation. **Said Quqa:** Writing – review & editing, Writing – original draft, Visualization, Validation, Methodology, Investigation, Formal analysis, Conceptualization. **Francesco Ubertini:** Writing – review & editing, Supervision. **Cristina Gentilini:** Writing – review & editing, Supervision, Conceptualization.

Declaration of competing interest

The authors declare the following financial interests/personal relationships which may be considered as potential competing interests: Said Quqa reports financial support was provided by European Union. If there are other authors, they declare that they have no known competing financial interests or personal relationships that could have appeared to influence the work reported in this paper.

Acknowledgments

This study was carried out within the MOST – Sustainable Mobility National Research Center and received funding from the European Union–Next Generation EU (PIANO NAZIONALE DI RIPRESA E RESILIENZA (PNRR) – MISSIONE 4 COMPONENTE 2, INVESTIMENTO 1.4 – D.D. 1033 del 17/06/2022, CN00000023). This manuscript reflects only the authors' views and opinions, and the Ministry cannot be considered responsible for them.

Appendix A. Investigation of mean displacement variations

For comparison with a traditional SHM approach, Fig. A.19 presents an alternative damage indicator for the real segments considered in this study. This indicator is calculated as the evolution of the mean displacement obtained from the PSs of each segment (corresponding to f_1 in Table 3), adjusted by subtracting the mean displacement of the baseline interval. Two thresholds are plotted, representing positive and negative 3 standard deviations of this damage indicator within the baseline interval.

The key differences observed compared to the proposed DI are: (1) some plots exhibit clear periodic trends driven by environmental factors (e.g., segment 2 15-IW3 and segment 4 15-IW3); (2) most plots show a decreasing trend over time (all segments except segment 2), likely reflecting a general displacement of the entire area, which is not critical for structural condition if uniform; (3) segment 2 appears stable over time. The effects described in points (1) and (2) are removed in the proposed DI, as only outliers from the general trend are identified as "anomalous".

Moreover, the anomalies identified in segments 1 and 2 (settlement and uplift, respectively) are not immediately apparent in these plots. The lack of visibility of the settlement in segment 1 may be due to its impact on other statistical moments more than on the mean displacement, which is similar to that of the other segments. In contrast, the absence of the uplift anomaly in segment 2 could be explained by one portion of the structure experiencing uplift while the other portion follows the general trend of decreasing displacement, resulting in a mean displacement that fluctuates around zero.

Thus, interpreting structural behavior solely by examining mean displacements in specific areas is not straightforward. To properly detect and interpret anomalies using this approach, it would be necessary to calculate displacements for smaller parts of the structure. However, the limited ground resolution of PSs in medium-resolution InSAR data poses a significant challenge to such localized analyses.

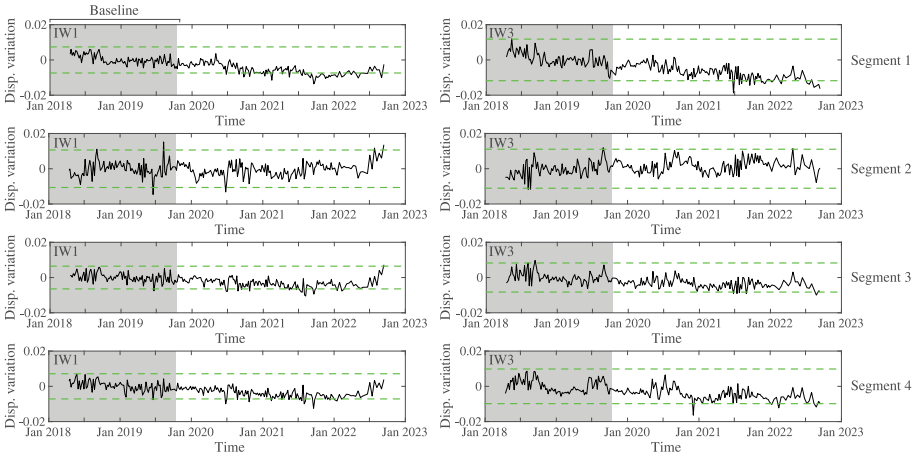

Fig. A.19. Mean displacement variation from the baseline interval.

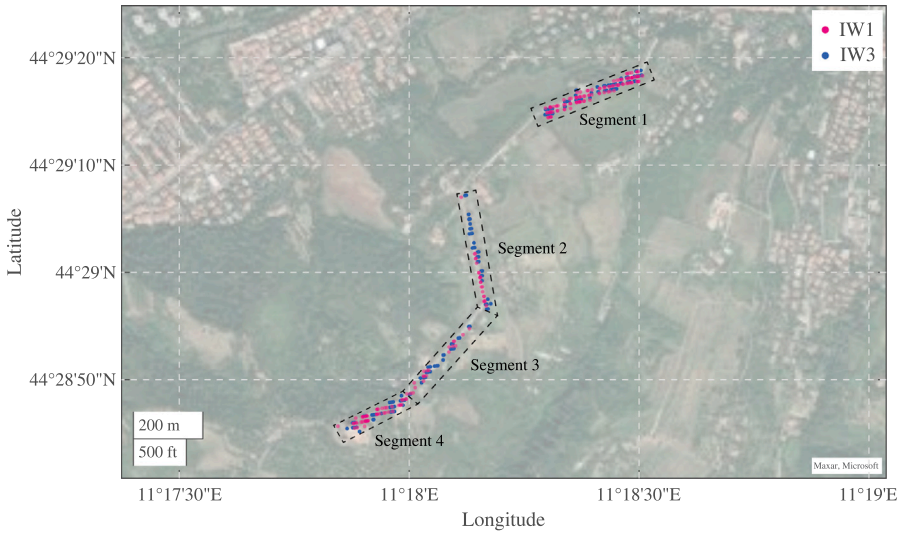

Fig. B.20. Persistent scatterers (PSs) of the displacement data for the 2019–2023 interval (tracks 117-IW1 and 15-IW3).

Appendix B. Analysis of the interval 2019–2023

For validation purposes, the proposed method was also applied to another dataset obtained for the interval from January 2, 2019, to December 25, 2023, available on the EGMS portal. Notably, while this interval partially overlaps with the one presented in the rest of the paper, the displacement data differ, as they were obtained by applying the PS-InSAR algorithm with different master images and calibration parameters [14,23]. The distribution of PSs has slightly changed, as shown in Fig. B.20. In these analyses, the baseline condition is taken from the previous dataset (shown in gray in Fig. 15), along with the threshold value.

Fig. B.21 presents the DI obtained for the new dataset, where an increasing trend is observed for segments 1 and 2 in both satellite tracks, starting at the same time as discussed in Section 6. Additionally, Fig. B.22 shows that segment 1 continues to exhibit settlement, progressing to the second intensity level by the end of 2023. Meanwhile, the initial signs of uplift in segment 2 are confirmed, with more recurrent anomalies observed in the new interval.

Data availability

Data will be made available on request.

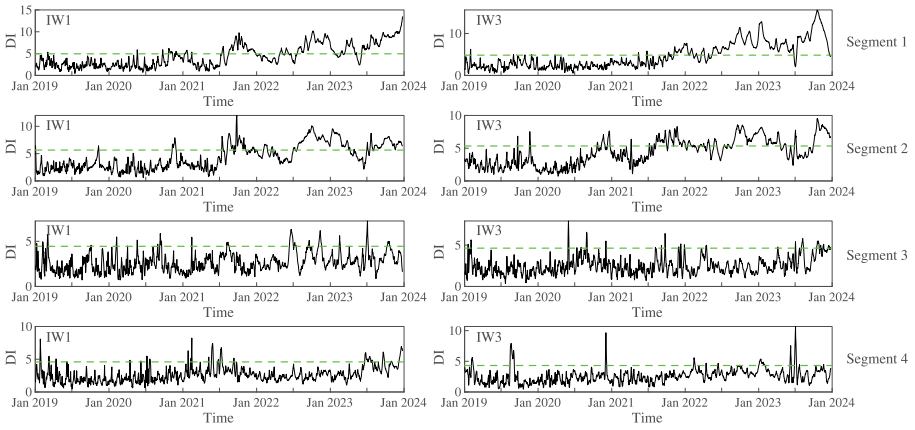

Fig. B.21. Damage index evaluated for the monitored segments during the 2019–2023 interval.

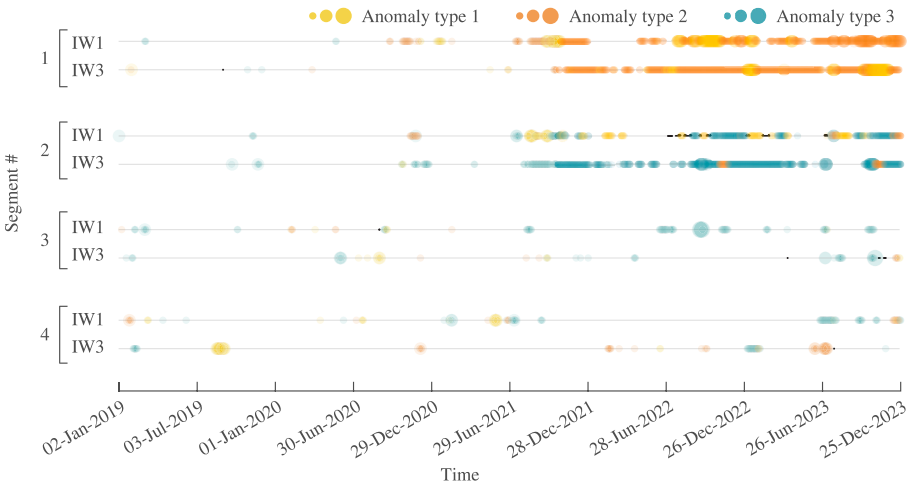

Fig. B.22. Classification results for the 2019–2023 interval.

References

[1] C. Gentile, A. Saisi, Ambient vibration testing of historic masonry towers for structural identification and damage assessment, Constr. Build. Mater. 21 (6) (2007) 1311–1321.

[2] L.F. Ramos, L. Marques, P.B. Lourenço, G. De Roeck, A. Campos-Costa, J. Roque, Monitoring historical masonry structures with operational modal analysis: Two case studies, Mech. Syst. Signal Process. 24 (5) (2010) 1291–1305.

[3] F. Ubertini, N. Cavalagli, A. Kita, G. Comanducci, Assessment of a monumental masonry bell-tower after 2016 central Italy seismic sequence by long-term SHM, Bull. Earthq. Eng. 16 (2018) 775–801.

[4] A. Kita, N. Cavalagli, F. Ubertini, Temperature effects on static and dynamic behavior of Consoli Palace in Gubbio, Italy, Mech. Syst. Signal Process. 120 (2019) 180–202.

[5] V. Gagliardi, L.B. Ciampoli, F. D'Amico, A.M. Alani, F. Tosti, A. Benedetto, Multi-temporal SAR interferometry for structural assessment of bridges: The rochester bridge case study, in: Airfield and Highway Pavements 2021, ASCE Library, 2021, pp. 308–319, http://dx.doi.org/10.1061/9780784483510.028.

[6] A. Ferretti, C. Prati, F. Rocca, Nonlinear subsidence rate estimation using permanent scatterers in differential SAR interferometry, IEEE Trans. Geosci. Remote Sens. 38 (5) (2000) 2202–2212, http://dx.doi.org/10.1109/36.868878.

[7] A. Ferretti, C. Prati, F. Rocca, Permanent scatterers in SAR interferometry, IEEE Trans. Geosci. Remote Sens. 39 (2001) 8–20, http://dx.doi.org/10.1109/36.898661.

[8] A. Ferretti, A. Monti-Guarnieri, C. Prati, F. Rocca, D. Massonnet, InSAR Principles: Guidelines for SAR Interferometry Processing and Interpretation, ESA Publications, 2007.

[9] S. Selvakumaran, S. Plank, C. Geiß, C. Rossi, C. Middleton, Remote monitoring to predict bridge scour failure using interferometric synthetic aperture radar (inSAR) stacking techniques, Int. J. Appl. Earth Obs. Geoinf. 73 (2018) 463–470, http://dx.doi.org/10.1016/j.jag.2018.07.004.

[10] A.M. Alani, F. Tosti, L.B. Ciampoli, V. Gagliardi, A. Benedetto, An integrated investigative approach in health monitoring of masonry arch bridges using GPR and inSAR technologies, NDT E Int. 115 (2020) 102288, http://dx.doi.org/10.1016/j.ndteint.2020.102288.

[11] G. Bonaldo, A. Caprino, F. Lorenzoni, F. da Porto, Monitoring displacements and damage detection through satellite MT-inSAR techniques: A new methodology and application to a case study in Rome (Italy), Remote. Sens. 15 (5) (2023) http://dx.doi.org/10.3390/rs15051177.

[12] E. Farneti, N. Cavalagli, M. Costantini, F. Trillo, F. Minati, I. Venanzi, F. Ubertini, A method for structural monitoring of multispan bridges using satellite inSAR data with uncertainty quantification and its pre-collapse application to the Albiano-Magra Bridge in Italy, Struct. Health Monit. 22 (1) (2023) 353–371, http://dx.doi.org/10.1177/14759217221083609.
[13] E. Farneti, N. Cavalagli, I. Venanzi, W. Salvatore, F. Ubertini, Residual service life prediction for bridges undergoing slow landslide-induced movements combining satellite radar interferometry and numerical collapse simulation, Eng. Struct. 293 (2023) 116628, http://dx.doi.org/10.1016/j.engstruct.2023.116628.
[14] A. Ferretti, E. Passera, R. Capes, End-to-End Implementation and Operation of the European Ground Motion Service (EGMS): Algorithm Theoretical Basis Document, Technical Report EGMS-D3-ALG-SC1-2.0-006, 2023.
[15] S. Quqa, A. Palermo, F. Ubertini, A. Marzani, Regional-scale bridge condition monitoring using inSAR displacements and environmental data, Struct. Health Monit. 24 (4) (2024) http://dx.doi.org/10.1177/14759217241302369, 14759217241302369.
[16] S. Quqa, O. Lasri, G. Delo, P.F. Giordano, C. Surace, A. Marzani, M.P. Limongelli, Regional-scale bridge health monitoring: survey of current methods and roadmap for future opportunities under changing climate, Struct. Health Monit. 24 (4) (2025) http://dx.doi.org/10.1177/14759217241310525, 14759217241310525.
[17] S.J. Pan, Q. Yang, A survey on transfer learning, IEEE Trans. Knowl. Data Eng. 22 (10) (2010) 1345–1359, http://dx.doi.org/10.1109/TKDE.2009.191.
[18] P. Gardner, X. Liu, K. Worden, On the application of domain adaptation in structural health monitoring, Mech. Syst. Signal Process. 138 (2020) 106550, http://dx.doi.org/10.1016/j.ymssp.2019.106550.
[19] L. Cipriani, Il disegno del portico di San Luca, CLUEB, 2005.
[20] A. Cleri, Guida al Portico di San Luca: dal Meloncello al Santuario, Editrice Compositori, 2008.
[21] G. Saccone, La Madonna Grassa nel Portico di San Luca - Andrea Ferreri scultore / architetto, Ordine degli Architetti di Bologna, Bologna, Italy, 2017.
[22] EGMS, European ground motion service, 2025, https://egms.land.copernicus.eu/. (Accessed 16 March 2025).
[23] P. Kotzerke, R. Siegmund, J. Langenwalter, End-to-End Implementation and Operation of the European Ground Motion Service (EGMS): Product User Manual, Technical Report EGMS-D4-PUM-SC1-2.0-007, 2022.
[24] ESA, Sentinel-1B In-Flight Anomaly Summary Report, Technical Report, 2022.
[25] J. Muñoz-Sabater, E. Dutra, A. Agustí-Panareda, C. Albergel, G. Arduini, G. Balsamo, S. Boussetta, M. Choulga, S. Harrigan, H. Hersbach, B. Martens, D.G. Miralles, M. Piles, N.J. Rodríguez-Fernández, E. Zsoter, C. Buontempo, J.N. Thépaut, ERA5-land: a state-of-the-art global reanalysis dataset for land applications, Earth Syst. Sci. Data 13 (9) (2021) 4349–4383, http://dx.doi.org/10.5194/essd-13-4349-2021.
[26] A. Pepe, M. Bonano, Q. Zhao, T. Yang, H. Wang, The use of C-/X-Band time-gapped SAR data and geotechnical models for the study of Shanghai's ocean-reclaimed lands through the SBAS-DInSAR technique, Remote. Sens. 8 (11) (2016) http://dx.doi.org/10.3390/rs8110911.
[27] W. Alahmad, S. Quqa, A. Ugolini, C. Gentilini, Simplified parametric structural model for masonry porticoes and bridges, in: International Conference Mechanics of Masonry Structures Strengthened with Composite Materials, Springer, 2025, pp. 475–484.
[28] B.A. Güney, E. Caner, Thermal and hygric expansion characteristics of mortars and bricks used in the dome structures of Turkish Baths from 14th and 15th centuries, Constr. Build. Mater. 95 (2015) 757–761.
[29] J. Carmeliet, S. Roels, Determination of the moisture capacity of porous building materials, J. Build. Phys. 25 (3) (2002) 209–237, http://dx.doi.org/10.1106/109719602022835.
[30] M. Kumaran, J. Lackey, N. Normandin, F. Tariku, D. van Reenen, Heat, air, and moisture transport properties of several north American bricks and mortar mixes, J. Test. Eval. 32 (5) (2004) 383–389, http://dx.doi.org/10.1520/JTE12149.
[31] M. Raimondo, M. Dondi, F. Mazzanti, P. Stefanizzi, P. Bondi, Equilibrium moisture content of clay bricks: The influence of the porous structure, Build. Environ. 42 (2007) 926–932, http://dx.doi.org/10.1016/j.buildenv.2005.10.017.
[32] E. Franzoni, C. Gentilini, G. Graziani, S. Bandini, Compressive behaviour of brick masonry triplets in wet and dry conditions, Constr. Build. Mater. 82 (2015) 45–52, http://dx.doi.org/10.1016/j.conbuildmat.2015.02.052.
[33] R. Ramirez, B. Ghiassi, P. Pineda, P. Lourenço, Simulation of moisture transport in fired-clay brick masonry structures accounting for interfacial phenomena, Build. Environ. 228 (2023) 109838, http://dx.doi.org/10.1016/j.buildenv.2022.109838.
[34] Y. Bahammou, M. Kouhila, O. Babaharra, Z. Tagnamas, H. Lamsyehe, A. Lamharrar, R. Idlimam, Experimental and numerical study of the impact of ambient air humidity on mortar cement durability using a static gravimetric method, Heat Mass Transf. 60 (2024) 1–19, http://dx.doi.org/10.1007/s00231-023-03417-0.
[35] Regione Emilia-Romagna, The geology of bologna, 2024, URL: https://ambiente.regione.emilia-romagna.it/en/geologia/dissemination/publications/opuscoli/the-geology-of-bologna. (Accessed 13 February 2025).
[36] P. Pezowicz, K. Choma-Moryl, Moisture content impact on mechanical properties of selected cohesive soils from the Wielkopolskie Voivodeship southern part, Stud. Geotech. et Mech. 37 (4) (2015) 37–46, http://dx.doi.org/10.1515/sgem-2015-0043.
[37] W. Guo, S. Xu, T. Hong, S. Hao, G. Chen, Study of structural and compression properties of soft soils in Kunming at different moisture contents, Shock. Vib. 2023 (2023) 1–10, http://dx.doi.org/10.1155/2023/8618546.
[38] B. Fernando, A. Habrard, M. Sebban, T. Tuytelaars, Unsupervised visual domain adaptation using subspace alignment, in: Proceedings of the IEEE International Conference on Computer Vision, ICCV, 2013, pp. 2960–2967, http://dx.doi.org/10.1109/ICCV.2013.368.
[39] E. Fix, Discriminatory Analysis: Nonparametric Discrimination, Consistency Properties, vol. 1, USAF School of Aviation Medicine, 1985.
[40] C. Gentilini, E. Franzoni, S. Bandini, L. Nobile, Effect of salt crystallisation on the shear behaviour of masonry walls: An experimental study, Constr. Build. Mater. 37 (2012) 181–189.